



**HAL**  
open science

## Melting of basaltic lithologies in the Earth's lower mantle

Marzena A Baron, Guillaume Fiquet, Guillaume Morard, Francesca Miozzi, Imène Esteve, Béatrice Doisneau, Anna S. Pakhomova, Yanick Ricard, François Guyot

► **To cite this version:**

Marzena A Baron, Guillaume Fiquet, Guillaume Morard, Francesca Miozzi, Imène Esteve, et al.. Melting of basaltic lithologies in the Earth's lower mantle. *Physics of the Earth and Planetary Interiors*, 2022, 333, pp.106938. 10.1016/j.pepi.2022.106938 . hal-03853140v1

**HAL Id: hal-03853140**

**<https://hal.science/hal-03853140v1>**

Submitted on 21 Nov 2022 (v1), last revised 15 Nov 2022 (v2)

**HAL** is a multi-disciplinary open access archive for the deposit and dissemination of scientific research documents, whether they are published or not. The documents may come from teaching and research institutions in France or abroad, or from public or private research centers.

L'archive ouverte pluridisciplinaire **HAL**, est destinée au dépôt et à la diffusion de documents scientifiques de niveau recherche, publiés ou non, émanant des établissements d'enseignement et de recherche français ou étrangers, des laboratoires publics ou privés.



Distributed under a Creative Commons Attribution - NonCommercial - NoDerivatives 4.0 International License

# 1 Melting of basaltic lithologies in the Earth's lower mantle

2

3 Marzena A. Baron<sup>a</sup>, G. Fiquet<sup>a</sup>, G. Morard<sup>a,b</sup>, F. Miozzi<sup>a\*</sup>, I. Esteve<sup>a</sup>, B. Doisneau<sup>a</sup>, A. Pakamova<sup>c</sup>  
4 Y. Ricard<sup>d</sup>, F. Guyot<sup>a</sup>

5

6 <sup>a</sup> Sorbonne Université, Institut de Minéralogie, de Physique des Matériaux et de Cosmochimie, Museum  
7 National d'Histoire Naturelle, UMR CNRS 7590, 75005 Paris, France;

8 <sup>b</sup> Université Grenoble Alpes, CNRS, ISTERRE, Grenoble, France ;

9 <sup>c</sup> Deutsches Elektronen-Synchrotron (DESY), Hamburg, Germany.

10 <sup>d</sup> Université de Lyon, ENSL, UCBL, Laboratoire LGLTPE, 15 parvis René Descartes, BP7000, 69342, Lyon,  
11 Cedex 07, France

12 <sup>\*Now at:</sup> Earth and Planets Laboratory, Carnegie Institution for Science, Washington, DC, USA

13

14

## 15 Abstract

16 As basaltic rocks formed at the base of the oceanic floor are transported back to the Earth's mantle along  
17 subduction zones, they undergo transitions and introduce compositional and thermal heterogeneities in the  
18 deeper parts of the mantle. Studying the melting phase relations of basaltic lithologies at elevated pressures  
19 and temperatures provides insights into what potentially happens at different depths in the lower mantle  
20 now and throughout the past billion years of active plate tectonics. Using laser heated - diamond anvil cell  
21 experiments combined with *in situ* X-Ray Diffraction measurements at synchrotron sources, we revisit the  
22 crystallization and melting properties of natural basaltic samples at 60-100 GPa and up to 4000 K.  
23 Diffraction patterns highlight the major phases: bridgmanite and Ca-perovskite, followed by crystallization  
24 of Si-rich phases (mainly stishovite) and Calcium Ferrite (CF-type) Na and Al-rich phase. Recovered samples  
25 were prepared using focused ion beam techniques for detailed chemical analyses of the extracted thin  
26 sections by electron microscopies in order to resolve sub-micron features and understand the chemical  
27 partitioning of elements induced by melting at high pressure and temperature conditions. We confirm that  
28 the liquidus phase is Ca-perovskite, which segregates during melting and is recovered as rings that  
29 encapsulate a melt pool throughout the studied pressure range. The melt pocket shows a concentric  
30 structure consisting of an alumino-silicate envelope surrounding an Fe-rich silicate part. At the center of  
31 samples, an Fe-O-S metal pond is often observed. We associate the observation of segregation of liquid  
32 phases to capillary forces. The differentiation of melt pockets into three melts is tentatively attributed to  
33 Marangoni effects, *i.e.* temperature-induced surface tension gradients in the samples. Central metal ponds  
34 are indirectly best interpreted as related to the disproportionation reaction of Fe<sup>2+</sup> into Fe<sup>3+</sup> and Fe<sup>(0)</sup>  
35 in bridgmanite whereas the two silicate-melt pools could be associated to the formation of two immiscible  
36 liquids upon melting of basalts. On the basis of these observations, we propose that melting of basaltic  
37 lithologies at lower mantle pressures could lead to important chemical differentiation mostly characterized  
38 by Fe enrichment at increasing depth.

39

## 40 Keywords:

41 basalt; Earth's lower mantle; X-ray diffraction; elemental partitioning; melting; laser heated diamond anvil  
42 cell, electron microscopy.

43

44

45

a mis en forme : Anglais (E.U.)

46 **1. Introduction**

47 The fate of basaltic and peridotitic material in the lower mantle has been a topic of experimental  
48 and computational research since decades. Linking geological observations of processes happening near  
49 and at the Earth's surface (*e.g.* volcanic activity and deep earthquakes related to the movement of the  
50 lithospheric plates) with seismic tomography images (*e.g.* van der Hilst et al., 1997; Fukao and Masayuki,  
51 2013), provides clear evidence of the dynamic nature of the Earth's interior. Furthermore, three-  
52 dimensional geodynamic simulations (*e.g.* Tackley et al., 1993; Nakagawa and Tackley, 2008) of the Earth's  
53 interior also support the concept of a whole-mantle convection. Thanks to advances in the geophysical  
54 observations of large- and small-scale heterogeneities in the Earth's mantle, we have now improved our  
55 understanding of the various plate tectonics setups, including different subduction scenarios and their role  
56 in the overall geodynamic cycle. Since the discovery of plate tectonics, it has been suggested that the oceanic  
57 plates undergo subduction into the deeper parts of the interior, but only just recently the different stages of  
58 this recycling process were captured (*e.g.* van der Meer et al 2018). Improved global mantle tomography  
59 models led to interpretations of lower-mantle slab structure and at this very moment, we have evidence of  
60 younger slabs briefly stagnating at depth between 660 and 1000 km (*e.g.* Caribbean slab under Lesser  
61 Antilles arc) and some older slabs already reaching the core-mantle boundary (*e.g.* Tonga-Kermadec-  
62 Hikurangi slab under Fidji). The present-day global mantle structure has also led to estimates of paleo-  
63 subduction zones and how that relates to our planet's dynamic evolution of the past ~300 Myr (*e.g.* Ricard  
64 et al., 1993, Torsvik et al. 2006, van der Meer et al. 2010).

65 Although the averaged structure of the bulk mantle resembles the mineralogy of peridotite with  
66 major phase transitions associated with the seismically resolvable discontinuities at 410 and 660 km depth,  
67 a more heterogeneous picture emerges from a detailed study of the geophysical data. The subducted mid-  
68 ocean ridge basaltic (MORB) material is different from the ambient lower mantle and therefore introduces  
69 chemical and thermal heterogeneities. One of the most distinct features in the lowermost part of the Earth's  
70 mantle is the laterally and vertically heterogeneous D' zone near the CMB (core-mantle boundary, *e.g.*  
71 Garnero and McNamara, 2008, Lay et al 2008, Torsvik et al., 2010, 2016, Trønnes et al 2018). The origin,  
72 composition and properties of these heterogeneities remain uncertain and are a subject of multidisciplinary  
73 discussions. The two antipodal large low shear-wave velocity provinces (LLSVPs) located underneath Africa  
74 and the Pacific and more localized ultra-low velocity zones (ULVZs) may be a result of either fractional  
75 crystallization of the magma ocean during the earliest history of the Earth and/or the continued accretion  
76 of subducted basaltic oceanic crust at the CMB (*e.g.* Labrosse et al., 2007, McNamara et al., 2010, Elkins-  
77 Tanton 2012, Torsvik et al. 2016) or both. In order to test both hypotheses, a good understanding of the  
78 melting phase relations of peridotitic and basaltic compositions are required throughout the whole mantle  
79 pressure range.

80 Melting phase relations of basaltic and peridotitic lithologies have been studied experimentally in  
81 multi-anvil presses up to the upper-lower mantle boundary (25 GPa) and laser-heated diamond anvil cell  
82 (LH-DAC) melting experiments until core-mantle boundary (135 GPa). The LH-DAC experiments on natural  
83 multi-component peridotitic (*e.g.* Fiquet et al., 2010; Andraut et al., 2011; Nomura et al., 2014) and basaltic  
84 compositions (*e.g.* Hirose et al., 1999, Andraut et al., 2014; Pradhan et al., 2015, Tateno et al., 2018) yield a  
85 range of solidus and liquidus temperatures at lower mantle pressures. It has been so far difficult to

86 discriminate between the effects of bulk composition, the presence or absence of volatiles in starting  
87 materials, various experimental setups (*e.g.* pressure medium effect) and the different melting criteria and  
88 detection techniques used to establish the melting curves and correctly interpret the chemistry in the run  
89 products. It should also be noted that, in the early studies, the chemical characterization of recovered  
90 samples has only been partially addressed, mainly focusing on determination of partition coefficients of Fe,  
91 Si and Mg, due to difficulties with sample recovery and analytical limitations. More in-depth chemical  
92 investigations have been presented by Pradhan et al. (2015) and Tateno et al. (2018), who focused on the  
93 small zone between the melt pocket and the liquidus phase instead of the entire sample. Finally, systematic  
94 studies of chemically simpler systems were also carried in order to assess the stability and understand the  
95 melting behaviour of lower mantle phases and eutectics in the MgO-SiO<sub>2</sub>, MgO-FeO-SiO<sub>2</sub> and CaO-MgO-SiO<sub>2</sub>  
96 systems (*e.g.* Liebske and Frost, 2012, Boukaré et al., 2015, Baron et al. 2017, Nomura et al. 2017 and Nabei  
97 et al., 2021).

98 Here, we present the results of our newest experimental and analytical study of melting natural  
99 basaltic lithologies at pressures of the Earth's lower mantle. We combined laser-heated diamond anvil cell  
100 (LH-DAC) experiments performed at 60-100 GPa and 3000-4000 K, with *in situ* synchrotron-based X-ray  
101 diffraction (XRD) measurements as well as multistep *ex situ* characterization of recovered samples using  
102 focused ion beam (FIB) preparation for analyses of chemistry and textures with electron microscopies. Our  
103 main goal in the present study is to constrain the issues of crystallization sequence, elemental distribution  
104 between melts and crystalline material, by testing various experimental setups and pressure media, and to  
105 interpret the complex quenched features of the LH-DAC experiments. This will allow us to finally  
106 understand the mechanisms of the recycling of the basaltic lithologies back in the lower mantle. In the end,  
107 we will also present potential physical explanation for melt segregation which commonly occurs in the LH-  
108 DAC experiments when melting occurs and which has been poorly described so far, possibly resulting in  
109 misleading interpretations of melt features and their chemistry.

110

## 111 2. Experimental and Analytical Methods

### 112 2.1. Starting Composition and Pressure Media

113 The starting composition used in this study was a natural MORB glass from the East Pacific Rise, where  
114 new oceanic crust is being formed. In **Table 1** the chemical composition of our starting material is listed  
115 together with examples of other basaltic samples, which were used in previously published experiments.  
116 Our basaltic material is relatively rich in minor elements like S, Mn, K and Na (see **Table 1**, (E)) but overall,  
117 major elemental concentrations are similar to other standards used in the literature. Glassy pieces  
118 homogeneous in compositions were extracted from geological thin sections (10-20 µm thick) and placed in  
119 between two discs of previously prepared pressure medium substances (PM). We have used two types of  
120 PM: crystalline KCl and amorphous Al<sub>2</sub>O<sub>3</sub>. Dried grains of KCl were cold pressed into sheets out of which  
121 disks of selected diameters were pre-cut by a femto-second laser and stored at 125°C to avoid moisture.  
122 The amorphous Al<sub>2</sub>O<sub>3</sub> was deposited using physical vapour deposition methods (see details in Morard et al.,  
123 2017). The discs served not only as pressure transmitting media and thermal insulators but also as reliable  
124 pressure calibrants. The PM-sample-PM sandwiches were then loaded in a pre-indented rhenium gasket  
125 (initially 200 µm thick) prepared for 'Princeton-type' symmetric DACs, with drilled holes of 80, 55 and 35

126  $\mu\text{m}$  for diamonds with flat culets of 200  $\mu\text{m}$  and beveled culets of 150/300 and 100/300- $\mu\text{m}$  diameters,  
 127 respectively. A small ruby sphere was added on the side of the sample chamber, away from the centre of  
 128 the basaltic sample for pressure measurement during compression. Before pressurising, the loaded but not  
 129 closed DACs were heated for an hour at 125°C to remove any absorbed moisture during loading  
 130 manipulations.

**Table 1.** Chemical composition of basaltic lithologies used in high-pressure and high-temperature experimental studies.

	BIR-1 standard	(A) + (B)	(C)	(D)	(E) + this study
SiO <sub>2</sub>	47.96	49.64	51	50.73	49.74
TiO <sub>2</sub>	0.96	1.64	1.7	2	1.33
Al <sub>2</sub> O <sub>3</sub>	15.5	14.88	15.7	13.73	15.89
FeO	10.4	11.43	9.9	11.29	9.73
MgO	9.7	8.51	7.7	6.76	8.46
CaO	13.3	10.55	11.2	10.94	11.74
Na <sub>2</sub> O	1.82	2.9	2.4	2.83	2.69
K <sub>2</sub> O	0.03	0.12	0.2	0.15	0.1
P <sub>2</sub> O <sub>5</sub>	0.021				0.11
MnO	0.175	0.18		0.2	0.18
S				0.15	0.14
Cr <sub>2</sub> O <sub>3</sub>					0.04
Total	99.866	99.85	99.8	98.78	100.15

(A) Hirose et al 1999; (B) Tateno et al 2018; (C) Ono et al 2005; (D) Andraut et al 2014;  
 (E) Pradhan et al 2015.

131  
 132

## 2.2. LH-DAC Experiments with *in-situ* X-Ray Diffraction Measurements

133 All experiments were performed using the laser-heated diamond anvil cell (LH-DAC) system installed  
 134 at the P02.2 Extreme Conditions Beamline (ECB) at Petra III in the Deutsche Elektronen Synchrotron (DESY)  
 135 (Liermann et al., 2015) in order to collect *in situ* X-ray diffraction (XRD) patterns.

136 At the synchrotron P02.2 beamline, the monochromatic beam of 42.65 KeV ( $\lambda = 0.2907 \text{ \AA}$ ) was focused  
 137 on a sample area of about 6  $\mu\text{m} \times 4 \mu\text{m}$ . The diffraction signal was collected on a PerkinElmer detector with  
 138 an exposure time between 5 and 10 s. Laser heating experiments were performed with an on-axis double-  
 139 sided laser heating setup equipped with a 200 W Yb-fibre laser which was split by a polarizing beam splitter  
 140 into two Gaussian profile beams (upstream and downstream). Typical laser spot size was ~10-20  $\mu\text{m}$  in  
 141 diameter. The emitted light from the laser-heated sample was then collected from both sides by a system of  
 142 mirrors and lenses and guided to the spectrograph entrance slit and CCD camera (Andor technology). The  
 143 transfer function of the optical system for temperature measurement was calibrated using a tungsten  
 144 halogen lamp at 2200, 2500 and 2900 K. Spectra from hot samples were used for temperature estimation  
 145 by fitting procedure to the Planck's law using the software T-Rax by C. Prescher. The error on the  
 146 temperature measurement was on the order of  $\pm 150 \text{ K}$ , which results from the measurement uncertainties,  
 147 including temperature gradients, heating instability, and accuracy of the grey body approximation.

148 Sample to detector distance and detector orientation were calibrated with a cerium dioxide (CeO<sub>2</sub>)  
 149 standard. Collected diffraction images were radially integrated using the software Dioptas (Prescher and  
 150 Prakash 2015) and analysed with the diffraction software PDIndexer (Seto et al. 2010).  
 151

152 The cells were pressurised to the target pressures at room temperature before laser-heating, using the  
153 R1 ruby fluorescence peak shift measurements (Mao et al., 1986). During each experiment, pressure was  
154 directly measured from the XRD pattern of the pressure transmitting media. The reported pressures in this  
155 study are always the post-heating measurements based on the quenched XRD patterns of KCl (Dewaele et  
156 al 2012) or Al<sub>2</sub>O<sub>3</sub> (Dewaele et Torrent, 2013). No correction was made for the thermal pressure effect.

157 The temperature in each experiment was first adjusted by levelling the laser power and coupling and  
158 focusing the lasers until both sides were at similar temperatures. Then the laser power was gradually  
159 increased on each side with a steady time increment until the target temperature (usually at or slightly  
160 above solidus  $\pm 150$  K, Pradhan et al 2015) was reached. Our goal was to induce melting but to keep the  
161 lowest degree of melting as possible. Therefore, as the laser power was ramped up, and after reaching the  
162 solidus temperature the experiment was finished and rapidly quenched by switching off the lasers. In few  
163 cases, we noticed a jump in the temperature to the solidus temperatures directly. All samples enclosed in  
164 the recovered gaskets containing the heated, recrystallized and melted basaltic lithologies were  
165 subsequently decompressed and kept under vacuum until further manipulation.

166

### 167 2.3. FIB sample preparation for SEM and TEM observations

168 The recovered DAC samples were transferred to a Zeiss Neon40EsB focused ion beam FIB-SEM system  
169 and characterised by Zeiss Ultra 55 field emission gun scanning electron microscope cope (FEG-SEM) and  
170 Jeol 2100F transmission electron microscope (TEM) at the IMPMC in Paris, France. The flat and indented  
171 culet areas of the Re-gaskets were first cut out by femto-second laser in a shape of half-moon (**Fig. 1a**) and  
172 fixed on the edge of a clean and flat silicon wafer piece with C-conductive glue (**Fig. 1b**). The silicon wafer  
173 was then placed in the middle of the alumina SEM-stub covered with a Cu-conductive tape and subsequently  
174 carbon coated before FIB milling. On top of the selected region of interest we deposited a Pt stripe of about  
175 2  $\mu\text{m}$  thickness. The FIB system at IMPMC allows electron imaging during the milling, enabling detection of  
176 the hot-spot area of the sample with high precision. When the quenched melts were exposed in an axial  
177 section from one side, the milling was continued from the other side. Thereby, we were able to locate the  
178 centre of the laser-heated hot spot, observe similar proportions of the quenched melt on both sides and  
179 prepare relatively thick (2-3  $\mu\text{m}$ ) and large (20-30  $\mu\text{m}$ ) section for extraction (**Fig. 1c**). The axial cuts were  
180 made through the entire thickness of the LH-DAC samples (15-30  $\mu\text{m}$ ) with the FIB gallium beam operating  
181 at different acceleration voltages (10, 5 and 2 kV). During the milling, we reduced the initial current of 10  
182 nA for efficient and fast milling to about 1 nA current for more precise cutting of the sample surfaces, then  
183 reducing further to 100-200 pA current for fine polishing in order to decrease Ga-implantation from the  
184 gun. The pre-cut sample sections were covered with a deposited 2  $\mu\text{m}$  Pt strip and subsequently hitched to  
185 the remotely manipulated needle by Pt-welding (**Fig. 1d**), cut off the gasket and lifted from the Re-gaskets  
186 (**Fig. 1e**). Then, the sample was transferred and mounted onto a copper TEM grid, where final thinning and  
187 cleaning of the sample surface took place (**Fig. 1f-h**). The thick lamellas resulting from this preparation  
188 were used for imaging and chemical analyses, performed with the FEG-SEM. The copper grids with samples  
189 were mounted as flat as possible on the special STEM (Scanning Transmission Electron Microscopy)  
190 alumina holder (**Fig. 1i**) in order to achieve reliable chemical analyses with minimum background effect.  
191 All the chemical analyses were carried out at 15 kV accelerating voltage and 10-20 nA beam current.

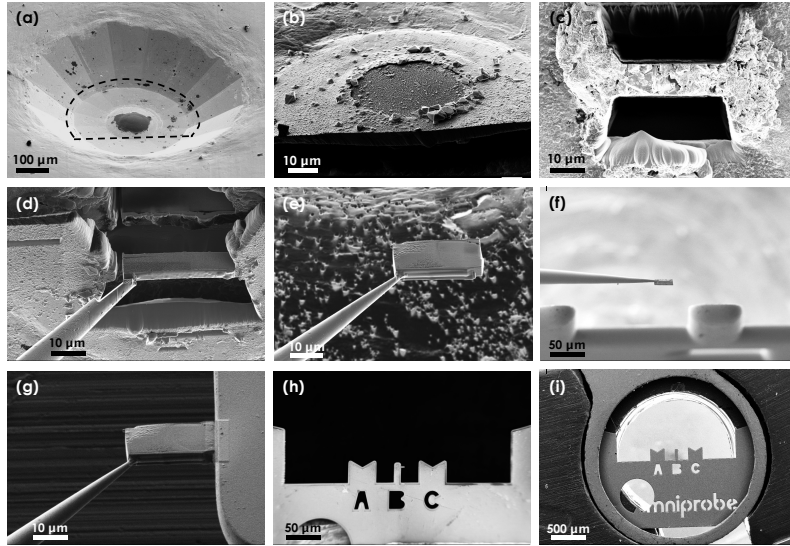


**Fig. 1.** Scanning electron images of the LH-DAC sample retrieval processes using focused ion beam (FIB) and scanning electron microscope (SEM). In short, the preparation starts with the sample decompression **(a)**, Re-gasket cutting with laser driller **(b)**, followed by large cuts with FIB **(c)** until the hotspot is found on both sides of the feature, Pt deposition on the thick lamella of interest **(d)**, extraction of the lamella using micro-manipulating W-needle **(e-f)** and attachment to the TEM Cu-grid **(g)** for further thinning and cleaning on the TEM Cu grid **(h)** in order to later perform high quality chemical analyses using SEM **(i)**, EMPA or TEM (more in the main text).

193

194

195

196

197

198

199

200

201

202

203

204

205

206

207

208

Further preparation was then required to prepare the samples for the TEM observations. To achieve the electron transparency, we further thinned the extracted lamellae down to about 150-200 nm thickness. We decided to thin half of the hot-spot areas as the features were very symmetric and large enough for the detailed investigation with the TEM microscope.

The TEM observations were carried with a Jeol 2100 F transmission electron microscope operating at 200 kV, equipped with a field effect gun, a high-resolution UHR pole piece, a Gatan US4000 CCD camera, and an energy-dispersive X-ray (EDX) analysis system from Jeol, which allowed us to perform electron diffraction and imaging as well as elemental maps in STEM mode.

Analysis by FE-SEM has been used in the most recent LH-DAC metal-silicate partitioning studies (*e.g.* Pradhan et al 2015 and Tateno et al 2018). We followed the same elaborated procedures of sample preparation (**Fig. 1a-c**) on all of our samples and we selected the centre of the heated area for lamella extraction and detail chemical analyses (SEM and TEM) samples. We used similar analytical conditions as described in the most recent publications to obtain elemental maps of the heated spots. However, it is worth mentioning that the electron microscopy analyses of the DAC samples need to be interpreted with caution and remain challenging due to potential analytical errors associated with the small size of the analysed

209 material (*e.g.* Wade and Wood, 2012). The contribution of secondary fluorescence arising from the  
210 neighbouring phases, the effect of sample thickness and a relatively large beam size, unable to resolve all  
211 the quenched features, are examples of the potential sources of analytical errors. The sample thickness is  
212 especially crucial for analyses of low-atomic number silicates in which the primary X-Ray excitation depth  
213 is greater than that of metals. With the lamella extraction and careful thinning, we can provide more  
214 accurate results and improve the current understanding of the chemistry of observed features on the sub-  
215 micron scale. Doing analytical TEM on FIB sections on this system and finding essentially similar results  
216 makes us confident that the results obtained here are robust.

217

### 218 3. Results

#### 219 3.1. XRD *in situ* in LH-DAC

220 The LH-DAC experiments were performed with basaltic starting compositions (Table 1) at around 60-  
221 70 and 90-100 GPa reaching temperatures above solidus (Andrault et al., 2014 and Pradhan et al., 2015) in  
222 order to ensure melting, necessary for studying solid-liquid elemental partitioning and melting phase  
223 relations. Upon laser-heating, we commonly observed a distinct perturbation, in the form of temperature  
224 plateaus in the temperature vs. laser power curve. Temperature plateaus are well known as good indicators  
225 of melting, and are especially well resolved during invariant melting of metals but are also useful to  
226 determine the melting of various silicates (*e.g.* Shen and Lazor, 1995; Anzellini et al., 2013; Lord et al.,  
227 2014a; Walter et al., 2015; Pradhan et al., 2015; Baron et al., 2017). As the starting material used in the  
228 present study and in Pradhan et al. (2015) was indeed the same natural basaltic glass (see **Tab. 1**), our  
229 melting experiments were performed in accordance with the Pradhan et al (2015) protocol where the first  
230 appearance of a diffuse scattering together with a jump in T and further temperature plateau was employed  
231 as a melting criterion. Here, once we reached the solidus temperature reported by Pradhan et al 2015, we  
232 rapidly quenched the experiments in order to study first melts and low-degree of melting in further sample  
233 recovery studies.

234 In **Fig. 2** we present the typical diffraction patterns collected before and during laser heating at PETRA,  
235 DESY. All cold diffraction patterns (before even turning on the lasers) show no peaks as expected from an  
236 amorphous starting material, however we can detect the typical broad feature (so called 'bump') in the  
237 diffuse scattering pattern of the glassy starting material which suggests short-order structure of the silicate  
238 glasses around  $9.0 \text{ } 2\theta$  (**Fig. 2**). The signal from the KCl pressure transmitting media is observed before  
239 and throughout the heating cycles (**Fig. 2 top**). The amorphous  $\text{Al}_2\text{O}_3$  pressure medium gives no detectable  
240 signal in the room temperature (cold) diffraction pattern likely because of very small size of coherently  
241 diffracting domains of the deposited pressure medium. Once the lasers start to heat the sample,  $\text{Al}_2\text{O}_3$  re-  
242 crystallizes and peaks corresponding to the pressure medium throughout the heating cycles can be  
243 observed (**Fig. 2 bottom**).

244 Collected XRD data allowed us to detect the co-existing phases, crystallizing from the amorphous  
245 basaltic glass during the experiment. In all high temperature and high pressure diffraction patterns we  
246 notice the immediate appearance of two main phases: bridgmanite ( $(\text{Mg,Fe})\text{SiO}_3$ ) and Ca-perovskite  
247 ( $\text{CaSiO}_3$ ). With further heating, we detect crystallization of stishovite ( $\text{SiO}_2$ ) and of a CaFe-type Al-rich phase  
248 (see **Fig. 2 top** and **bottom**). These four crystalline phases have been also reported in all the previously

249 published LH-DAC with *in-situ* XRD studies performed at similar pressure and temperature conditions  
 250 (Andraut et al., 2014; Pradhan et al., 2015, Tateno et al., 2018).  
 251  
 252 Our results of XRD patterns in sub-solidus conditions are therefore in good agreement with Andraut et al.,  
 253 2014; Pradhan et al., 2015, Tateno et al., 2018, although the experimental setups of all these experiments

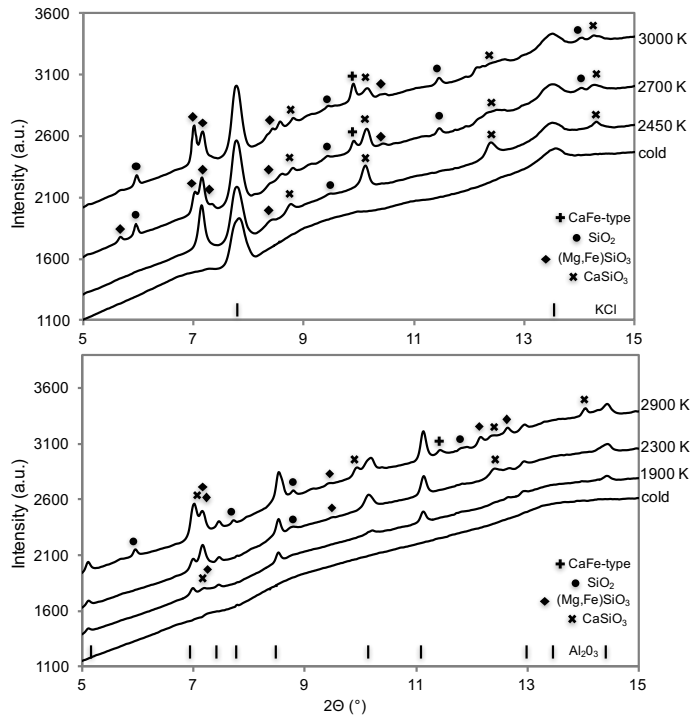


**Fig. 2.** *In situ* XRD patterns of the LH-DAC experiments made with the natural basalts using two different types of pressure medium: **top:** KCl - #12\_P9\_2 basalt at 65 GPa; **bottom:** Al<sub>2</sub>O<sub>3</sub> - #8\_Z3\_2 basalt at 65.5 GPa. The cold diffraction patterns were collected at room temperature and show no peaks from the sample except the distinctive bump from the amorphous glass.

254 were different. Moreover, despite of using two different types of pressure media, we observed exactly the  
 255 same phase relations in the diffraction patterns at high pressure-temperature conditions. In all experiments  
 256 we also observed a jump in temperature at the solidus line; however, the fast quenching prevented us to  
 257 detect the diffuse scattering signal from the small liquid portion generated during the experiment.

258

### 259 3.2. Chemical mapping of concentric differentiated structures in the samples

260 A concentric structure with different layers of distinct chemical compositions (**Fig. 3** and **4**, **Tab. 2**) is  
 261 observed in all the experiments. When we progressively approach the hot-spot area from the outside of the  
 262 heated zone, we see in 2D a first outer ellipse growing when advancing the milling. It is composed of grains  
 263 whose sizes increase towards the centre of the heated zone (**Fig. 2** and more in **Fig. S3** of supplementary

264 **materials**). Then a second ellipsoid of the amorphous Ca-pv composition emerges and leads us to the centre  
265 of the last zone which itself contains two ellipsoids made of very homogeneous material without visible  
266 grains, and finally a small blob very iron-rich more or less at the center of the samples. The central blob is  
267 made of an Fe-S-O phase surrounded by an ellipsoid of a homogeneous phase highly enriched in iron and  
268 aluminium compared to the composition of the initial basaltic glass, and then the next ellipsoidal ring going  
269 toward the outside of the hotspot is made of a phase enriched in silicon and aluminum compared to the  
270 initial basaltic glass. Considering the strong compositional difference between the starting material and the  
271 materials in those two ellipsoids and in the central blob, we consider that they are melts constitutive of a  
272 central melt pocket that will be discussed further on. The quenched textures and general features of our  
273 recovered samples are similar to those observed in previous basaltic melting studies (*e.g.* Pradhan et al.,  
274 2015 and Tateno et al., 2018). In **Fig. 3** we summarise the typical BSE electron images and SEM elemental  
275 maps of the major elements: Si, Mg, Fe and O. More elemental distribution maps of Al, Na, Ti, S, K and Cl can  
276 be found in the supplementary materials (**Appendix A**). We find no contamination from the surrounding  
277 medium as the small heated area has been protected by the unreacted glassy sample from the pressure-  
278 medium and therefore even at high temperature neither reaction nor elemental diffusion has occurred. We  
279 also do not see the typical effects of the Soret diffusion (Sinmyo et Hirose, 2010), where Fe would escape  
280 the hottest area in the centre of the laser-heated spot.

281 In general, in all experiments performed around 60-70 GPa (**Fig. 2a-b**) we notice that the central melt  
282 pool consists of the three described component (Fe-O-S blob, Fe-enriched and Fe-poor silicate melts).  
283 However, in few higher-pressure experiments above 100 GPa (**Fig. 2c**) the melt pool exhibits more  
284 homogeneous appearance but overall similar elemental partitioning characteristics. In few cases, in co-  
285 existence with the melt pocket we have also captured crystals of stishovite or Ca-perovskite trapped in the  
286 melt matrix (**Fig. 2b**).

287 In **Fig. 4** and **Appendix B** Energy Dispersive X-ray maps acquired at high magnification in the TEM can  
288 be found together with electron images of the whole reacted areas. Based on this more detailed TEM  
289 observations we confirm that the quenched Fe-poor melt is usually very homogeneous and fine-grained on  
290 all scales (**Fig. 4b**) with a glassy appearance, suggesting rapid quenching of the silicate material. The  
291 quenched texture of the Fe-rich melt is also chemically very homogeneous (like in **Fig. 3a** and **b**) but in the  
292 nano-scale observations we notice needlelike microstructures at the boundary with the Fe-poor melt and  
293 more nano-scale quenched textures (**Fig. 4b**). As revealed by TEM, the Fe-blobs in the centre consist actually  
294 of FeO and FeS domains (**Fig. 4a**) and the boundary with Fe-rich melt is remarkably distinctive. Similar  
295 metal alloys melts have been previously observed and have been featured in run products from large  
296 volume press (LVP) experiments (*e.g.* O'Neil et al., 1998; Ricolleau et al., 2011 and Siebert et al., 2011) and  
297 previous LH-DAC as well (*e.g.* Fiquet et al., 2010; Frost et al., 2010 and Siebert et al., 2012). Around the melt  
298 pool, the CaSiO<sub>3</sub> ring, which in SEM pictures resembles a glassy homogeneous texture but in the TEM images,  
299 as in **Fig. 4c**, we can detect the nano-scale grains with CaSiO<sub>3</sub> - SiO<sub>2</sub> domains. In contact with this CaSiO<sub>3</sub>  
300 large areas, the basalt starting glassy material has recrystallized into (Mg,Fe)SiO<sub>3</sub> perovskite (bridgmanite)  
301 CaSiO<sub>3</sub> - perovskite (amorphized) and SiO<sub>2</sub> (stishovite). In the recrystallised subsolidus zone examined by  
302 TEM, we have also detected distinctive crystals of Calcium Ferrite (CF-type) Na and Al-rich phase in sub-  
303 micron scale which can be found in the supplementary materials (**Appendix C**). These phases have already

304 been described in previous experiments on similar samples (Ricolleau et al., 2010). All of the subsolidus  
305 phases found in the FIB sections have also been confirmed in the X-ray diffraction patterns (Fig. 2).  
306

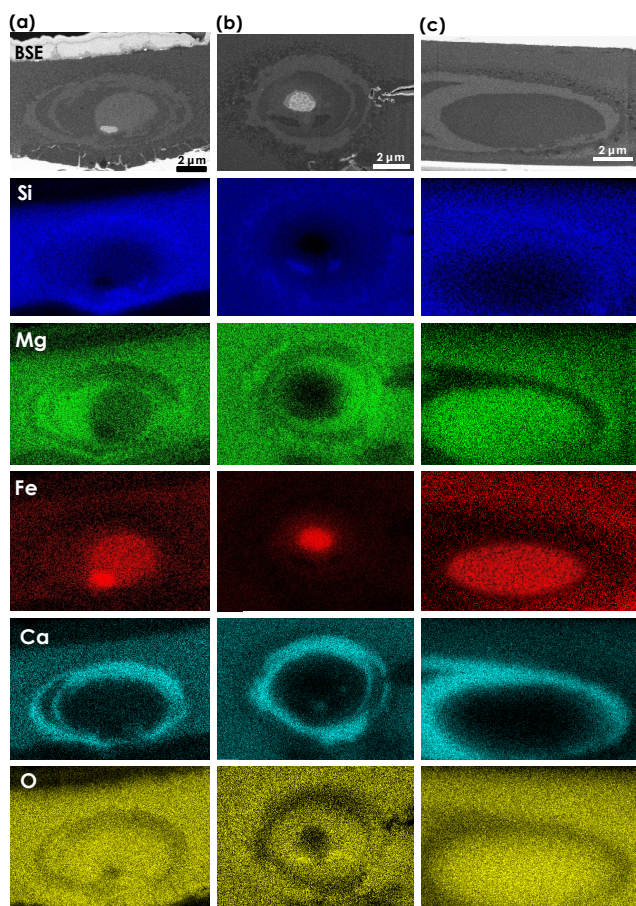


**Fig. 3.** EDX elemental maps and BSE/SE images of the melting experiments of natural basalt, **(a)** - #12\_P9\_2 65 GPa, **(b)** - #8\_M3\_1 65.5 GPa, **(c)** - #6\_P6\_2 101 GPa.

307 Carbon contamination through diffusion from diamond anvils was not observed, and the relatively  
308 high totals of the microprobe analyses suggest very low C-contribution. This was probably a result of the  
309 pressure-medium acting as a chemical barrier between the basaltic glass and diamond anvils.

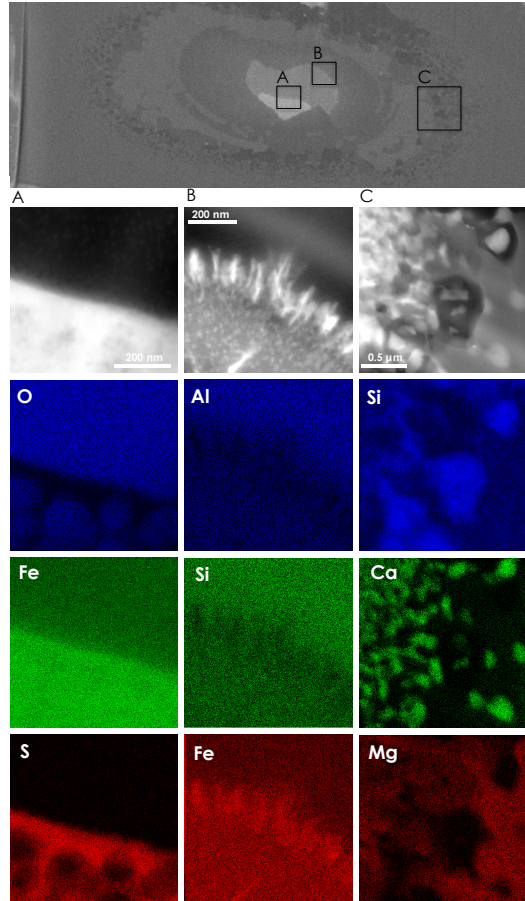


**Fig. 4.** TEM STEM elemental maps and electron images of the melting experiment of natural basalt (#2\_basalt at 64 GPa). The three regions of interest show three types of interfaces between A: metallic melt and Fe-rich melt; B: Fe-rich melt and silicate melt; C: Ca-perovskite and sub-solidus recrystallisation of a basaltic phases: SiO<sub>2</sub> stishovite, (Mg,Fe)SiO<sub>3</sub> bridgmanite and small grains of CaSiO<sub>3</sub>.

310 From the SEM and TEM chemical observations on the micro and nanoscale, respectively, we have  
 311 extracted the chemical compositions of coexisting phases in the hotspots, summarized in **Table 2**. We also  
 312 compare analyses made on two samples which were melted at similar pressure (~ 65 GPa) in experiments  
 313 performed using either Al<sub>2</sub>O<sub>3</sub> or KCl pressure medium. We notice no significant difference in the chemical  
 314 compositions of all the prominent components of the experimental assembly, the metallic blob, Fe-poor  
 315 and Fe-rich melts, Ca-pv and Mg-pv (**Table 2**). However due to the small size of the crystalline phases (e.g.  
 316 MgPv on the outskirts of the large Ca-pv layer in the sample #12 in KCl) we notice that analyses made by the  
 317 EDX-TEM on the very thin lamellas provide more reliable chemical composition than EDX-SEM data which

318 were made on thicker lamellas, where the effect of the excitation depth may alter the observations (Table  
 319 2).  
 320

**Table 2.** Chemical compositions of coexisting phases in the hotspots.

Run #8 in Al <sub>2</sub> O <sub>3</sub>					Run #12 in KCl						
Pressure		65.5 GPa				Pressure		65 GPa			
		melts						melts			
Phase		Si-rich	Fe-rich	CaPv	MgPv	Phase		Si-rich	Fe-rich	CaPv	MgPv
SEM	SiO <sub>2</sub>	43.40	28.99	52.33	42.83	SEM	SiO <sub>2</sub>	38.15	33.04	52.09	61.29
wt%	TiO <sub>2</sub>	2.17	4.63		1.21	wt%	TiO <sub>2</sub>	2.09	5.83	1.24	0.60
	Al <sub>2</sub> O <sub>3</sub>	25.66	23.37	7.09	16.09		Al <sub>2</sub> O <sub>3</sub>	30.10	20.50	5.87	15.43
	FeO	11.02	33.61	6.19	7.55		FeO	15.55	34.61	5.02	5.80
	MgO	13.53	4.30	4.10	17.99		MgO	7.59	1.76	5.98	6.71
	CaO	3.05	3.02	30.05	11.11		CaO	2.77	1.44	27.91	7.14
	Na <sub>2</sub> O	1.21	2.14		2.44		Na <sub>2</sub> O	2.99	2.75	1.81	2.84
	Total	100.04	100.06	99.76	99.22		Total	99.24	99.93	99.92	99.81
		melts						melts			
		Si-rich	Fe-rich	CaPv	MgPv			Si-rich	Fe-rich	CaPv	MgPv
TEM	SiO <sub>2</sub>	45.15	16.99	47.39	42.30	TEM	SiO <sub>2</sub>	44.06	20.95	49.44	46.01
wt%	TiO <sub>2</sub>	2.45	4.43	1.46	1.56	wt%	TiO <sub>2</sub>	2.02	9.13	1.52	1.48
	Al <sub>2</sub> O <sub>3</sub>	24.45	12.77	1.15	15.14		Al <sub>2</sub> O <sub>3</sub>	21.00	14.68	1.98	21.82
	FeO	12.39	60.15	7.72	19.30		FeO	11.20	51.34	5.42	10.36
	MgO	12.78	2.83	2.74	18.31		MgO	12.48	0.48	3.20	17.77
	CaO	1.96	2.07	39.39	2.34		CaO	8.13	1.81	37.85	1.95
	Na <sub>2</sub> O	0.81	0.77	0.15	1.05		Na <sub>2</sub> O	1.11	1.61	0.59	0.61
	Total	100.00	100.00	100.00	100.00		Total	100.00	100.00	100.00	100.00

321  
 322 In addition, we have also summarised the experimental chemical data obtained in the previously published  
 323 literature in **Appendix D** and we see similar chemical compositions of all the major crystalline phases,  
 324 however in order to directly compare the melt compositions we suggest to use a model which we describe  
 325 later (see **Table 3** ).  
 326

### 3.3. Remarks on the pressure medium (PM)

327  
 328 In order to understand further effects due to pressure medium on LH-DAC melting experiments we  
 329 used KCl or amorphous Al<sub>2</sub>O<sub>3</sub> discs as a pressure medium, pressure calibrant, and thermal insulator. Based  
 330 on our *in situ* XRD and elemental maps of the recovered samples we notice that using a thin layer of pressure  
 331 medium, either KCl or Al<sub>2</sub>O<sub>3</sub>, does not interfere with the crystallization sequence and partitioning behaviour  
 332 of the elements. No matter what material we used as the pressure medium, the diffraction patterns of the  
 333 heated basaltic samples show the same phases crystallizing from the homogeneous glass. Experiments with  
 334 KCl were particularly successful as sodium chloride structure is cubic with well identified peaks that did  
 335 not overlap with the X-ray diffraction signal from the sample. In case of an Al<sub>2</sub>O<sub>3</sub> pressure medium, the  
 336 heated amorphous glass crystallized during LH-DAC experiment, which on one hand serves as a robust  
 337 internal pressure calibrant but on the other hand strongly diffracts, masks signal from the sample and  
 338 makes the interpretation of XRD patterns more challenging. The laser heating has been very efficient as the  
 339 pressure medium was acting as an efficient thermal insulator, preventing the heat loss through the  
 340 conductive diamond anvils. A lot of attention has to be made to the post-experimental preparation of  
 341 samples because the heating spot has to be kept smaller than the size (thickness) of the glassy silicate  
 342 sample, *i.e.* the hot spot ideally is still surrounded by unreacted glassy zone which we have documented

343 further in the supplementary materials (**Appendix E**). As soon as there was a mechanical contact between  
 344 the melt and pressure medium a reaction can occur which contaminates the primary starting composition  
 345 and influences the partitioning relations. In the perspective of previous LH-DAC experiments, although in  
 346 the Andraut et al., 2014 KCl pressure medium has also been used, we have obtained results closer to the  
 347 more recent studies in which no pressure transmitting media was used, and the region of interest has been  
 348 preserved within the bulk unheated glassy starting material (Pradhan et al. 2015 and Tateno et al 2018).

#### 350 4. Discussion

##### 351 4.1. Calcium silicate perovskite as the liquidus phase in melting of basaltic compositions

352 In all our experiments, we report a concentric structure made of successive rings with a geometry of  
 353 revolution ellipsoids (**Fig 5**) which obviously correspond to the hot spot of the laser with less efficient  
 354 heating when approaching the diamond in any plane containing the laser axis (**Fig. 5**). In all planes the  
 355 structure of the samples is evolving isotropically because the projection of the hot spot is an elongated  
 356 perpendicular to the compression axis sphere, with a gaussian temperature profile. Outside of the elliptical  
 357 hot spot, one finds unreacted glassy starting material, then transformed material with increasing grain sizes  
 358 when moving toward the center of the samples (*e.g.* **Fig. 5d** and **e**). This sequence is most likely associated  
 359 with a subsolidus assemblage in those areas of the laser-heated spot in which temperature was not  
 360 sufficient for melting. Then the other inner rings or ellipsoids have bulk chemistries very different from the  
 361 starting material and are most likely associated to melting. The outermost of these rings is dominated by a

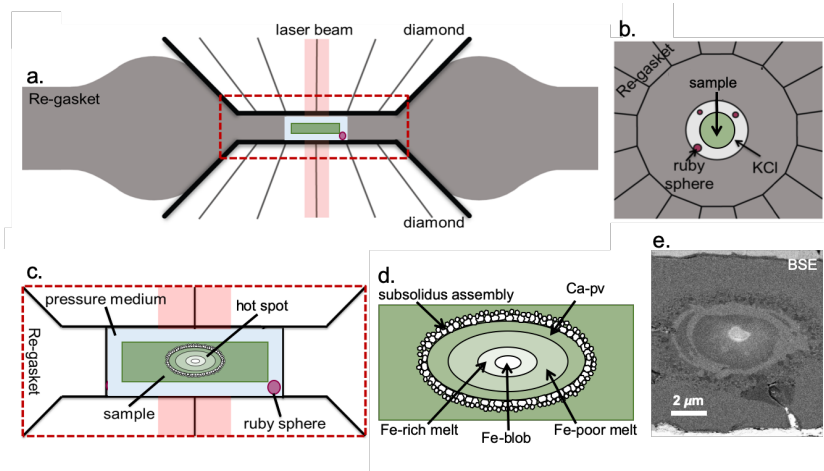


**Fig. 5.** Schematic diagrams of the LH-DAC experimental assembly: **(a)** with respect to the position of diamonds, Re-gasket, laser beams (red shaded), **(b)** a top view of the experimental setup in the Re-gasket **(c)** a typical cross section showing the experimental setup with a sample that has been heated and melted with lasers at high pressure, surrounded by KCl/Al<sub>2</sub>O<sub>3</sub> pressure medium and ruby sphere inside the sample chamber of the pre-indented Re-gasket **(d)** magnified view of the typical result of the high pressure and high temperature experiments after quenching showing the observed and described in this study melt structures (Fe-poor, Fe-rich and Fe-blob), liquidus phase (Ca-pv) and the subsolidus assembly: recrystallisation of a basaltic phases surrounded by unreacted glassy sample **(e)** BSE image of the hot spot area in one of our experiments, for comparison.

362 composition close to CaSiO<sub>3</sub>. This leads us to state that CaSiO<sub>3</sub> perovskite (cpv) is the last solid phase to melt  
363 (liquidus phase) and thus the first to crystallize in a crystallization sequence. It is very likely that once  
364 formed upon temperature elevation, the melt migrates towards the center of the sample (see discussion  
365 below) forming the innermost ellipsoidal rings and blob. Previously published studies on basaltic melts  
366 compositions in the lower mantle pressure regime agree that the crystallization sequence is first cpv as the  
367 liquidus phase, followed by stishovite (stv) or modified stishovite (CaCl<sub>2</sub>-structured) and then bridgmanite  
368 bm (Andraut et al., 2014; Pradhan et al., 2015; Tateno et al., 2018). This behaviour does not drastically  
369 change over a large pressure range. At pressures exceeding 108 and 123 GPa, the crystallization sequence  
370 of a basaltic melt has been reported to be cpv-bm-silica and cpv-pbm-silica, respectively (Tateno et al.,  
371 2018). Seifertite (SiO<sub>2</sub> with α-PbO<sub>2</sub> structure) likely replaces modified stishovite (CaCl<sub>2</sub>-structured silica)  
372 as the silica phase near the solidus at lowermost mantle conditions. At lower pressures, based on multi-  
373 anvil press experiments, Hirose and Fei (2002) found that cpv and stishovite crystallize almost  
374 simultaneously at 23-24 GPa, but that cpv is clearly the liquidus phase, preceding stishovite at slightly  
375 higher pressures of 25-28 GPa.

376 For a comparison, the crystallization sequence of natural peridotite at pressures above 30-40 GPa  
377 is different, with bridgmanite (bm) as the liquidus phase, followed by ferropericlase (fp) and then cpv as a  
378 solidus phase (Fiquet et al. 2010; Andraut et al., 2011; Tateno et al., 2014; Nomura et al., 2014; Nabei et al.,  
379 2021). This clearly distinguishes the consequences of melting of the two most discussed Earth's mantle  
380 lithologies.

#### 381 382 **4.2 Iron enrichment of melts.**

383 We subsequently used electron microscopy on recovered run products to better understand the  
384 melting phase relations and quenched textures captured during the high-pressure and high temperature  
385 experiments. The Fe-S and Fe-O phases observed in the center of the samples (**Fig. 3 and 4**) are most likely  
386 quenched textures of a Fe-S-O metallic melt. The abundance of this metallic melt is very low. The most likely  
387 interpretation of this melt is that it could be related to the products of the bridgmanite disproportionation  
388 reaction (*e.g.* Frost et al. 2004) and coalesce in the centre of the experimental charge as melting develops  
389 (see discussion of melt migration below).

390 Then moving outwards from the sample centre, two ellipsoidal zones with very different chemical  
391 composition than that of the starting material are observed, corresponding to melts both enriched in Al, one  
392 of the two melts being very depleted in Si and very enriched in Fe (**Table 2**). It is possible that these two  
393 melts correspond to two liquid phases appearing successively during the temperature rise and then  
394 migrating immediately once formed, or to an immiscibility in the liquid state already observed several times  
395 during basalt melting studies at lower pressure (*e.g.* Vincenzi et al 1995; Veksler et al. 2007). It is interesting  
396 to combine the compositions of these two liquids using a first rough approximation which consists in  
397 ponderating their compositions by their surface proportions. In **Table 3** we present modelled melt  
398 compositions of two similar samples melted and quenched at around 65 GPa but embedded in two different  
399 pressure media (#12\_P9\_2 in Al<sub>2</sub>O<sub>3</sub> and #8\_M3\_1 in KCl ). Using the BSE images and chemical maps (**Fig. 3**)  
400 we estimate the fraction of the Fe-poor and Fe-rich melt and we use the chemical compositions of the two  
401 components (presented in **Table 2**). We thus obtain an average liquid resulting from basalt fusion (**Table**

3) whose composition is strongly enriched in Al and Fe compared to the composition of the initial basalt glass. This is consistent with the results of several previous studies which showed that upon high pressure melting of basalts, the silicate melts are enriched in FeO relative to the solid starting material (see Fig 3) reflecting preferential partitioning of FeO into the melt (e.g. Corgne et al., 2008; Tateno et al., 2014; and Pradhan et al 2015). Andrault et al 2014 showed results in which melts are Si-enriched at the highest pressures of the lower mantle (120 GPa), however in the intermediate pressures (38-80 GPa) such enrichment is not evident. Considering the segregation of melts observed in our experiments, we propose that an iron-rich melt might have remained undetected in Andrault et al 2014 highest pressure experiments due to type of sample preparation and chemical observation made from the top surface, without exposing the centre of the hotspot. In our approach of exposing the very centre of the hotspots, we gain a better control of the complex geometry of quench features. Also, the combination of SEM and TEM methods allows us to cross-check the robustness of the data.

**Table 3.** Modelled melt compositions

		#8	#12
fraction	Si-rich	0.56	0.87
	Fe-rich	0.44	0.13
SEM	SiO <sub>2</sub>	37.06	37.4857
wt%	TiO <sub>2</sub>	3.25	2.5762
	Al <sub>2</sub> O <sub>3</sub>	24.65	28.853914
	FeO	20.96	18.0278
	MgO	9.47	6.8321
	CaO	3.04	2.5971
	Na <sub>2</sub> O	1.62	2.9588
	Total	100.05	99.33
TEM	SiO <sub>2</sub>	32.76	41.0557
wt%	TiO <sub>2</sub>	3.32	2.94604
	Al <sub>2</sub> O <sub>3</sub>	19.31	20.1784
	FeO	33.41	16.4182
	MgO	8.40	10.92
	CaO	2.01	7.3084
	Na <sub>2</sub> O	0.79	1.175
	Total	100.00	100.00

414  
415  
416

#### 4.3. Understanding the melt segregation and concentric layers

The quenched samples of concentric features starting from the center: Fe-O-S melt, Fe-rich melt, Fe-poor melt, CaSiO<sub>3</sub> ring (liquidus phase), solidus assemblage, untransformed basaltic glass (Fig. 3 and 4). Similar observations of onion-rings have been made in previous basalt melting or peridotite melting studies at high pressure in laser heated diamond-anvil cell experiments. What are possible interpretations of these structures?

The intense laser heating induces instantaneously huge gradients of thermal pressure P and temperature T (of orders 0.1GPa/1μm and 100 K/1μm). A possible source of segregation of phases initially mixed could be due to the difference in their mechanical strengths. If one phase is less viscous than the other, its pressure will be more homogeneous. The interface between the phases of different properties will

426 then influence the local pressure environment leading the more viscous phase to the centre and expelling  
427 the less viscous phase away from the highest-pressure zone. This compaction mechanism should drain the  
428 less viscous phase from the hotspot (McKenzie, 1984; Ricard et al., 2001). This would yield a separation of  
429 phases with the most viscous phase (probably the silicate melt most depleted in Fe) at the centre, that  
430 appears opposite to what we observed.

431 The surface tension between phases,  $\sigma$  is certainly a major force at the micrometric scale  $r$  of these  
432 experiments as the ratio between surface tension and gravity forces is  $\sigma/\rho_0gr^2 \gg 1$ . The effect of surface  
433 tension is twofold. A first and usual effect of surface tension is associated to the curvature of the interface  
434 separating phases. This favours the formation of large bubbles by coalescence of smaller bubbles until the  
435 two phases self-separate (like oil and water). This mechanism should therefore lead to the separation of the  
436 different immiscible phases but cannot explain the embedded final position of these various phases.

437 A second effect of surface tension is related to the inhomogeneity of the temperature. This induces  
438 forces, called Marangoni forces (Marangoni, 1871), related to surface tension gradients rather than to  
439 interface curvature. These forces tend to drive the phase interfaces in the direction where the surface  
440 tension is lower. They act on the bubbles of the low viscosity phase and drive them to the center of the  
441 hotspot as surface tension is lower at high temperature (Young et al., 1959; Ricard et al., 2021). This effect  
442 is related to the product of the temperature derivative of surface tension  $\sigma'$  times the temperature gradient.  
443 There are not many experiments measuring  $\sigma'$  for phases relevant to the pressure and temperature  
444 conditions of the experiment but Terasaki et al. (2012) suggests  $\sigma' \approx -2 \text{ mN m}^{-1} \text{ K}^{-1}$ . Such a value implies  
445 that the self-separation and the Marangoni forces have similar amplitude as their ratio  $\sigma/(-\sigma'T) \approx 1$ . This  
446 importance of the Marangoni force in this experiment is of course due to the huge temperature gradient  
447 that is imposed.

448 It seems therefore that Marangoni forces with the likely conditions that the surface tension between  
449 metal and silicates is larger than between the metal-rich and metal-poor silicate melts, are able to segregate  
450 the liquid phases in the order indicated by the experiment. This segregation is helped by the more common  
451 aspect of capillary forces, leading to self-separation.

#### 452 4.4. Application of the observations in the Earth's mantle

453 Considering our new experimental data on melting phase relations and elemental partitioning at high  
454 pressure and temperatures relevant to the deep Earth, and in agreement with Pradhan et al., 2015, Tateno  
455 et al., 2018, we have confirmed that basaltic material which happens to reach the deepest part of the lower  
456 mantle will melt. The melting temperature of basaltic lithologies determined by Pradhan et al., 2015 and  
457 used in this work to target solidus temperatures for study of early melts (low degree melting) has been  
458 confirmed in our experiments. The Fe-, Al-, and Mg-rich melt will segregate leaving highly refractory Ca-pv  
459 behind which will lead to accumulation of these components at the bottom of the Earth's mantle. Such melts  
460 might potentially be the source of the ultra-low velocity zones (ULVZs) which have been detected locally on  
461 the edges of the large low-shear velocity provinces (LLSVPs) which dominate the D'' zone, just above the  
462 core mantle boundary (CMB).

463 The density and viscosity of the melts and crystal residuals at the extreme conditions of the CMB need  
464 to be studied further to understand their role in the overall structure, compositions, dynamics and evolution  
465 of the Earth's interior, potentially using novel experimental methods and atomistic calculations.

466

## 467 5. Conclusions

468 Reaching the high pressure-temperature conditions of the Earth's deep interior and particularly  
469 performing *in situ* experiments at synchrotron facilities provides the only way to sample and reconstruct  
470 the melting phase relations and crystallization sequences relevant to planetary geodynamics. Adding *ex situ*  
471 investigations of quenched melting experiments enables detailed solid-liquid elemental partitioning  
472 investigations. Studying basaltic samples at lower mantle conditions is therefore a shortcut into  
473 understanding the past events and present-day mantle heterogeneities, which are linked with the  
474 subduction zones.

475 Using LH-DAC experiments combined with *in situ* X-Ray Diffraction measurements at the synchrotron,  
476 we studied crystallization and melting of natural basaltic lithologies at 60-100 GPa and up to 4000 K. We  
477 decompressed and recovered samples to perform *ex situ* investigation using focused ion beam techniques  
478 (FIB) and electron microscopies (SEM and TEM) to map and visualize the heated zones and understand the  
479 chemical partitioning of elements induced by melting under high pressures and temperatures. We used  
480 pressure media (KCl and amorphous  $\text{Al}_2\text{O}_3$ ) to test the influence of this parameter on the results.

481 In the studied pressure range, all the diffraction patterns contained bridgmanite and Ca-perovskite  
482 crystallizing as major phases already at relatively low temperatures, with the increasing temperature  
483 crystallization of Si-phases (mainly stishovite) and CF-type Al- and Na-rich phase has been detected. The  
484 melting was assigned to the sudden jump in the temperature measurement around the solidus temperature  
485 in agreement with the Pradhan et al. 2015 melting curve.

486 Based on our chemical observations, we notice distinctive 'onion like' shells of various experimental  
487 products. In the middle, the melts are Fe-, Mg- and Al-rich and consist of Fe-poor and Fe-rich domains with  
488 small FeO+FeS metallic blobs linked with bridgmanite disproportionation reaction. The liquidus phase is  
489 Ca-perovskite, creating rings of nano-crystalline  $\text{CaSiO}_3$  that encapsulate the melt pool throughout the  
490 studied pressure range. In co-existence with the melt, we have also captured crystals of stishovite, Ca-  
491 perovskite. Towards the colder area we observe the characteristic sub-solidus assembly of sub-micron  
492 grains of bridgmanite, Ca-pv, stishovite and CF-structure Al- and Na-rich phase. No effect of the used  
493 pressure media on the melting phase relations, melting and elemental partitioning is noted. However, the  
494 laser-heating spot must be smaller than the thickness of the starting material to avoid contamination and  
495 preserve the unreacted glassy starting material around the hotspot.

496 Due to the complexity of the structure and composition of the melt pockets presented in LH-DAC  
497 experiments we have investigated the possible physical explanation of their formation. We described the  
498 potential impact of the temperature and pressure gradients, surface tension and Marangoni forces on the  
499 formation of the heterogeneous melt zones. It appears that the conjunction of capillary forces and  
500 temperature dependence of surface tension offer the best explanation of the observed arrangement of  
501 segregated melt phases.

502 Reflecting our experimental observation with the global view of the subducted basaltic lithologies back  
503 in the lower mantle we confirm that if basaltic material melts under lower mantle presumably in the deepest  
504 parts of the lower mantle close to the Core Mantle Boundary, Fe rich melt will be segregated downward.

505  
506  
507  
508  
509

#### 510 **Acknowledgements**

511 The research has been funded by the European Research Council (ERC) under the European Union's  
512 Horizon 2020 research and innovation Programme (grant agreement 670787, PlanetDive). The Focused Ion  
513 Beam (FIB) and Scanning Electron Microscope (SEM) facility at IMPMC are supported by Région Ile de  
514 France grant SESAME 2006 N°I-07-593/R, INSU-CNRS, Institut de Physique (INP)-CNRS, University Pierre  
515 et Marie Curie-Paris 6, and by the French National Research Agency (ANR) grant ANR-07-BLAN-0124-01.  
516 Femtosecond laser micromachining at the Institut de Minéralogie de Physique des Matériaux et de  
517 Cosmochimie (IMPMC), Paris, has been developed and realized by the "Cellule Project" with the financial  
518 support of ANR 2010-JCJC-604-01. The *in-situ* XRD measurements and LH-DAC experiments were carried  
519 out at beamline P02.2 at PETRA III at DESY, which is part of the Helmholtz Association (HGF).

520

#### 521 **References**

- 522 Andraut, D., Bolfan-Casanova, N., Nigro, G.L., Bouhif, M.A., Garbarino, G., Mezouar, M., 2011. Melting curve  
523 of the deep mantle applied to properties of early magma ocean and actual core-mantle boundary. *Earth  
524 Planet. Sci. Lett.* 304, 251–259.
- 525 Andraut, D., Pesce G., Bouhifd, M.A., Bolfan-Casanova, N., Hénot, J.-M., Mezouar, M., 2014. Melting of  
526 subducted basalt at the core-mantle boundary. *Science* 344 (6186), 892–895.
- 527 Anzellini, S., Dewaele, A., Mezouar, M., Loubeyre, P., Morard, G., 2013. Melting of iron at Earth's inner core  
528 boundary based on fast X-ray diffraction. *Science* 340 (6131), 464–466.
- 529 Baron, M.A., Lord, O.T., Myhill, R., Thomson, A.R., Wang, W., Trønnes, R.G., Walter, M.J., 2017. Experimental  
530 constraints on melting temperatures in the MgO-SiO<sub>2</sub> system at lower mantle pressures. *Earth Planet. Sci.  
531 Lett.* 472, 186–196.
- 532 Boukaré, C.E., Ricard, Y., Fiquet, G., 2015. Thermodynamics of the MgO-FeO-SiO<sub>2</sub> system up to 140 GPa:  
533 Application to the crystallization of Earth magma ocean. *J. Geophys. Res.*, 120 (9), 6085-6101.
- 534 Corgne, A., Keshav, S., Wood, B.J., McDonough, W.F., Fei, Y., 2008. Metal-silicate partitioning and constraints  
535 on core composition and oxygen fugacity during Earth accretion. *Geochim. Cosmochim. Acta* 72, 574–589.
- 536 Deweale, A., Belonoshko, A. B. Garbarino, G., Ocelli, F., Bouvier, P., Hanfland, M., Mezouar, M., 2012. High-  
537 pressure-high-temperature equation of state of KCl and KBr. *Phys. Rev. B* 85, 214105
- 538 Deweale, A., Torrent, M., 2013. Equation of state of  $\alpha$ -Al<sub>2</sub>O<sub>3</sub>. *Phys. Rev. B* 88, 064107.

- 539 Elkins-Tanton, L.D., 2012. Magma oceans in the inner Solar System. *Annu. Rev. Earth Planet. Sci.* 40, 113–  
540 139.
- 541 Fiquet, G., Auzende, A.L., Siebert, J., Corgne, A., Bureau, H., Ozawa, H., Garbarino, G., 2010. Melting of  
542 peridotite to 140 GPa. *Science* 329, 1516–1518.
- 543 Frost, D.J., Liebske, C., Langenhorst, F., McCammon, C.A., Tronnes, R.G., Rubie, D.C. 2004. Experimental  
544 evidence for the existence of iron-rich metal in the Earth's lower mantle. *Nature* 428, 409–412.
- 545 Frost, D.J., Asahara, Y., Rubie, D.C., Miyajima, N., Dubrovinsky, L.S., Holzapfel, C., Ohtani, E., Miyahara, M.,  
546 Sakai, T., 2010. The partitioning of oxygen between the Earth's mantle and core. *J. Geophys. Res.* 115,  
547 B02202.
- 548 Fukao, Y., Obayashi, M., 2013. Subducted slabs stagnant above, penetrating through, and trapped below the  
549 660 km discontinuity. *JGR Solid Earth* 118 (11), 5920-5938.
- 550 Garnero, E.J., McNamara, A.K., 2008. Structure and dynamics of Earth's lower mantle. *Science* 230, 626–628.
- 551 Hirose, K., Fei, Y., Ma, Y., Mao, H.-K. 1999. The fate of subducted basaltic crust in the Earth's lower mantle.  
552 *Nature* 397, 53-56.
- 553 Hirose, K., Fei, Y., 2002. Subsolvus and melting phase relations of basaltic composition in the  
554 uppermost lower mantle. *Geochim. Cosmochim. Acta* 66, 2099–2108.
- 555 Labrosse, S., Hernlund, J.W., Coltice, N., 2007. A crystallizing dense magma ocean at the base of the Earth's  
556 mantle. *Nature* 450, 866–869.
- 557 Lay, T., Hernlund, J., Buffett, B.A., 2008. Core-mantle boundary heat flow. *Nat. Geosci.* 1, 25-32.
- 558 Liebske, C., Frost, D.J., 2012. Melting phase relations in the MgO–MgSiO<sub>3</sub> system between 16 and 26 GPa:  
559 Implications for melting in Earth's deep interior. *Earth Planet. Sci. Lett.* 345-348, 159–170.
- 560 Liermann, H.P., Konôpková, Z., Morgenroth, W., Glazyrin, K., Bednarčík, J., McBride, E.E., Petitgirard, S.,  
561 Delitz, J.T., Wendt, M., Bican, Y., Ehn, A., Schwark, I., Rothkirch, A., Tischer, M., Heuer, J., Schulte-  
562 Schreppeing, H., Kracht, T., Franz, H., 2015. The Extreme Conditions Beamline P02.2 and the Extreme  
563 Conditions Science Infrastructure at PETRA III. *J. Synchrotron Radiat.* 22, 908–924.
- 564 Lord, O.T., Wann, E.T.H., Hunt, S.A., Walker, A.M., Santangeli, J., Walter, M.J., Dobson, D.P., Wood, I.G., Vočadlo,  
565 L., Morard, G., Mezouard, M., 2014. The NiSi melting curve to 70 GPa. *Phys. Earth Planet. Inter.* 233, 13–23.
- 566 Mao, H.K., Xu, J., Bell, P.M., 1986. Calibration of the ruby pressure gauge to 800-kbar under quasi-hydrostatic  
567 conditions. *J. Geophys. Res. Solid Earth* 91, 4673–4676.
- 568 Marangoni, C., 1871. Ueber die ausbreitung der tropfen einer flüssigkeit auf der oberfläche einer anderen.  
569 *Annalen der Physik*, 219(7):337–354.
- 570 McKenzie, D., 1984. The generation and compaction of partially molten rock. *J. Petrol.*, 25:713–765.
- 571 Allen K. McNamara, Edward J. Garnero, Sebastian Rost, 2010. Tracking deep mantle reservoirs with ultra-  
572 low velocity zones, *Earth and Planetary Science Letters*, Volume 299, Issues 1–2.

573 Nabei, F., Badro, J., Boukaré, Ch.-É., Hébert, C., Cantoni, M., Borensztajn, S., Wehr, N., Gille, P., 2021.  
574 Investigating Magma Ocean Solidification on Earth Through Laser-Heated Diamond Anvil Cell Experiments.  
575 *Geophysical Research Letters*, 48, e2021GL092446.

576 Nakagawa, T., Tackley, P.J., 2008. Lateral variations in CMB heat flux and deep mantle seismic velocity  
577 caused by a thermal-chemical-phase boundary layer in 3D spherical convection. *Earth Planet. Sci. Lett.* 271,  
578 348-358.

579 Nomura, R., Hirose, K., Uesugi, K., Ohishi, Y., Tsuchiyama, A., Miyake, A., Ueno, Y., 2014. Low core-mantle  
580 boundary temperature inferred from the solidus of pyrolite. *Science* 343, 522-525.

581 Nomura, R., Zhou, Y., Irifune, T., 2017. Melting phase relations in the MgSiO<sub>3</sub>-CaSiO<sub>3</sub> system at 24 GPa. *Prog.*  
582 *Earth Planet. Sci.* 4, 34.

583 O'Neil, H.St.C., Canil, D., Rubie, D.C., 1998. Oxide-metal equilibria to 2500°C and 25 GPa: implications for core  
584 formation and the light component in the Earth's core. *J. Geophys. Res.* 13, 12239-12260.

585 Ono, S., Ohishi, Y., Isshiki, M., Watanuki, T., 2005. In situ X - ray observations of phase assemblages in  
586 peridotite and basalt compositions at lower mantle conditions: Implications for density of subducted  
587 oceanic plate. *JGR: Solid Earth*, 110, B02208.

588 Pradhan, G.K., Fiquet, G., Siebert, J., Auzende, A.-L., Morard, G., Antonangeli, D., Garbarino, G., 2015. Melting  
589 of MORB at core-mantle boundary. *Earth Planet. Sci. Lett.* 431, 247-255.

590 Prescher, C., Prakapenka, V.B., 2015. DIOPTAS: a program for reduction of two-dimensional X-ray  
591 diffraction data and data exploration. *High Press. Res.* 35, 223-230.

592 Ricard, Y., Richards, M. A., Lithgow-Bertelloni, C., Lestunff Y., 1993. A Geodynamic Model of Mantle Mass  
593 Heterogeneities, *J. Geophys. Res.*, 98, 21895-21909.

594 Ricard, Y., Bercovici, D., Schubert, G., 2001. A two-phase model for compaction and damage 2. Applications  
595 to compaction, deformation, and the role of interfacial surface tension. *J. Geophys. Res.*, 106:8907-8924.

596 Ricard, Y., Labrosse, S., Terasaki, H., Bercovici, D., 2021. Thermocapillary effects in two-phase medium and  
597 applications to metal-silicate separation. *Physics of the Earth and Planetary Interiors*, 311, 106640.

598 Ricolleau, A., Fei, Y.W., Corgne, A., Siebert, J., Badro, J., 2011. Constraints on oxygen and silicon contents of  
599 Earth's core from metal-silicate partitioning experiments at high pressure and temperature. *Earth Planet.*  
600 *Sci. Lett.* 310, 409-421.

601 Seto, Y., Nishio-Hamane, D., Nagai, T., Sata, N. 2010. Development of a Software Suite on X-ray Diffraction  
602 Experiments. *The Review of High Pressure Science and Technology* 20(3):269-276

603 Shen, G., Lazor, P., 1995. Measurement of melting temperatures of some minerals under lower mantle  
604 pressures. *J. Geophys. Res.* 100 (B9), 17699-17713.

605 Siebert, J., Corgne, A., Ryerson, F.J. (2011) Systematics of metal-silicate partitioning for many siderophile  
606 elements applied to Earth's core formation. *Geochim. Cosmochim. Acta* 75(6), 1451-1489.

607 Siebert, J., Badro, J., Antonangeli, D., Ryerson, F.J. (2012) Metal-silicate partitioning of Ni and Co in a deep  
608 magma ocean. *Earth Planet. Sci. Lett.* 321-322, 189-197.

609 Sinmyo, R., Hirose, K., (2010) The Soret diffusion in laser-heated diamond-anvil cell. *Physics of the Earth*  
610 *and Planetary Interiors*. 180, 3–4, 172-178

611 Tackley, P.J., Stevenson, D.J., Glatzmaier, G.A., Schubert, G., 1993. Effects of an endothermic phase transition  
612 at 670 km depth in a spherical model of convection in the Earth's mantle. *Nature* 361, 699–704

613 Tateno, S., Hirose, K., Ohishi, Y., 2014. Melting experiments on peridotite to lowermost mantle conditions. *J.*  
614 *Geophys. Res. Solid Earth* 119, 4684-4694.

615 Tateno, S., Hirose, K., Sakata, S., Yonemitsu, K., Ozawa, H., Hirata, T., 2018. Melting Phase Relations and  
616 Element Partitioning in MORB to Lowermost Mantle Conditions. *Journal of Geophysical Research: Solid*  
617 *Earth*, 123(7), 5515–5531.

618 Terasaki, H., Urakawa, S., Rubie, D. C., Funakoshi, K.-i., Sakamaki, T., Shibasaki, Y., Ozawa, S., and Ohtani, E.,  
619 2012. Interfacial tension of Fe-Si liquid at high pressure: Implications for liquid Fe-alloy droplet size in  
620 magma oceans. *Phys. Earth Planet. Inter.*, 202:1–6.

621 Torsvik, T.H., Smethurst, M.A., Burke, K., Steinberger, B., 2006. Large Igneous Provinces generated from the  
622 margins of the large low velocity provinces in the deep mantle. *Geophys. J. Int.* 167, 1447–1460.

623 Torsvik, T.H., Burke, K., Steinberger, B., Webb, S.J., Ashwal, L.D., 2010. Diamonds sampled by plumes from  
624 the core–mantle boundary. *Nature* 466, 352-355.

625 Torsvik, T.H., Steinberger, B., Ashwal, L.D., Doubrovine, P.V., Trønnes, R.G., 2016. Earth evolution and  
626 dynamics – a tribute to Kevin Bruke. *Can. J. Earth Sci.*, 53, 1073-1087.

627 Trønnes, R.G., Frost, D.J., 2002. Peridotite melting and mineral-melt partitioning of major and minor  
628 elements at 22–24.5 GPa. *Earth Planet. Sci. Lett.* 197, 117–131.

629 Trønnes R.G., Baron M.A., Eigenmann K.R., Guren M.G., Løken A., Mohn C.E. 2018. Early melting and  
630 differentiation, Earth and terrestrial planets. *Tectonophysics*, Vol. 760, 1650-198.

631 van der Hilst, R.D., Widiyantoro, S., Engdahl, E.R., 1997. Evidence for deep mantle circulation from global  
632 tomography. *Nature* 386, 578–584.

633 van der Meer, D.G., van der Hinsbergen, D.J.J., Spakman, W., 2018. Atlas of the underworld: Slab remnants in  
634 the mantle, their sinking history, and a new outlook on lower mantle viscosity. *Tectonophysics* 723, 309-  
635 448.

636 Veksler, I.V., Dorfman, A.M., Borisov, A.A., Wirth, R., Dingwell, D.B., 2007. Liquid Immiscibility and the  
637 Evolution of Basaltic Magma. *Journal of Petrology*, 48(11), 2187-2210.

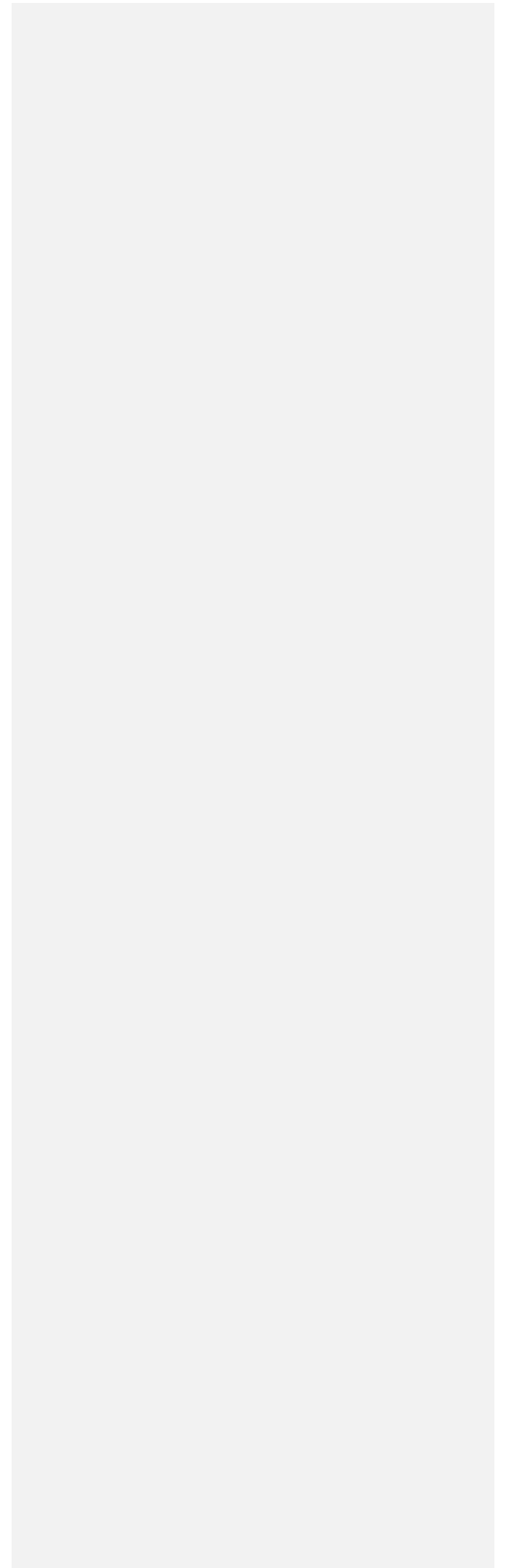
638 Vincenzi, E.P., Green, T.H., Sie, S.H., 1995. Immiscible silicate liquids at high pressure: The influence of melt  
639 structure on elemental partitioning. *Nuclear Instruments and Methods in Physics Research B* 104 (1995)  
640 470-475.

641 Walter, M.J., Thomson, A.R., Wang, W., Lord, O.T., Ross, J., McMahon, S.C., Baron, M.A., Melekhova, E., Kleppe,  
642 A.K., Kohn, S.C., 2015. The stability of hydrous silicates in Earth's lower mantle: experimental constraints  
643 from the systems MgO-SiO<sub>2</sub>-H<sub>2</sub>O and MgO-Al<sub>2</sub>O<sub>3</sub>-SiO<sub>2</sub>-H<sub>2</sub>O. *Chem. Geol.* 418, 16–29.

644 Young, N., Goldstein, J., and Block, M. 1959. The motion of bubbles in a vertical temperature gradient. *J. Fluid*  
645 *Mech.*, 6(3):350–356.

646  
647  
648  
649  
650  
651  
652  
653  
654  
655  
656  
657

**Supplementary materials**



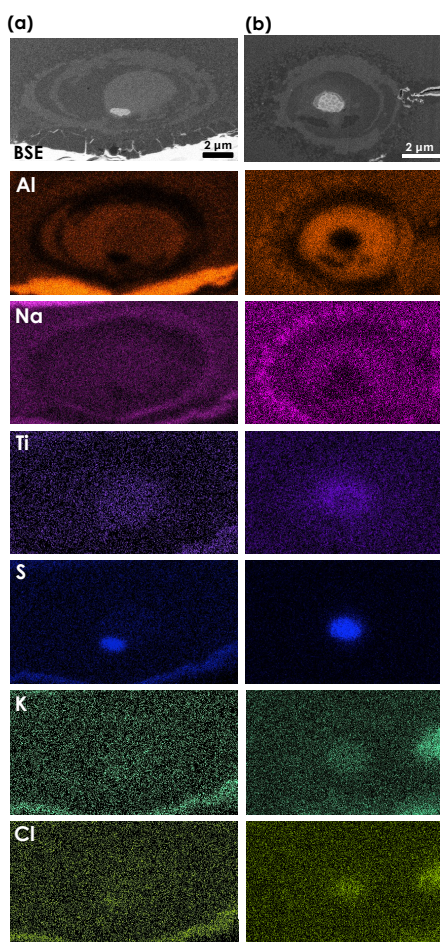


**Fig. S1.** BSE/SE images and EDX elemental maps of Al, Na, Ti, S, K and Cl of the melting experiments of natural basalt, **(a)** - #8\_M3\_1 65.5 GPa, **(b)** - #12\_P9\_2 GPa encapsulated by the unreacted basaltic glasses (starting material). The scale bar in (a) applies to all four images.

659

660

661

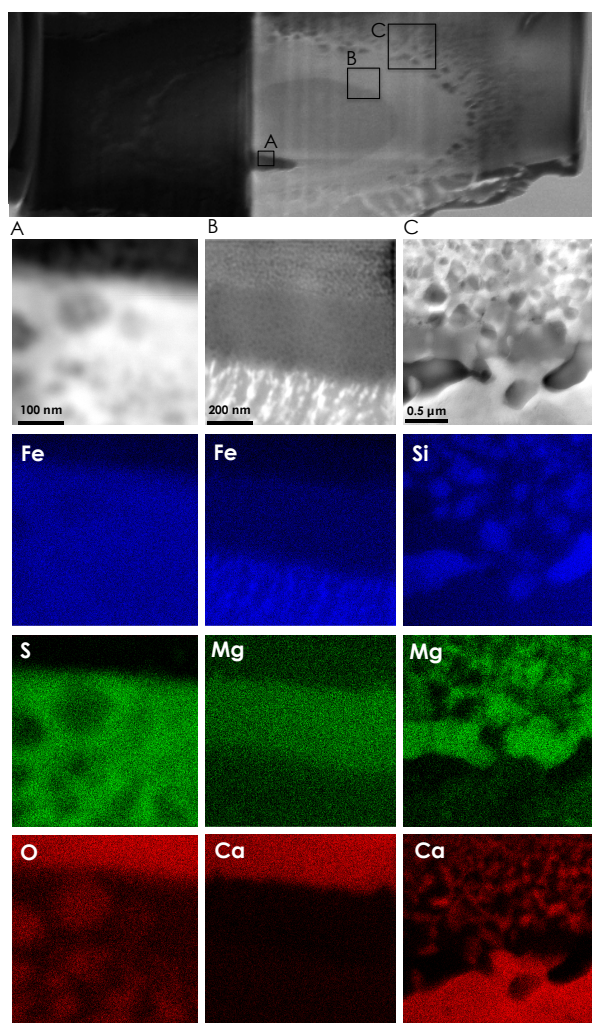


**Fig. S2.** TEM STEM elemental maps and electron images of the melting experiment of natural basalt (#8\_basalt at 65.5 GPa). The three regions of interest show all the types of interfaces between **A**: metallic melt and Fe-rich melt; **B**: Fe-rich melt and silicate melt and silicate melt and Ca-perovskite ring; **C**: Ca-perovskite ring and sub-solidus recrystallisation assembly of a basaltic phases: SiO<sub>2</sub> stishovite, (Mg,Fe)SiO<sub>3</sub> bridgmanite and some CaSiO<sub>3</sub> (Ca-perovskite).

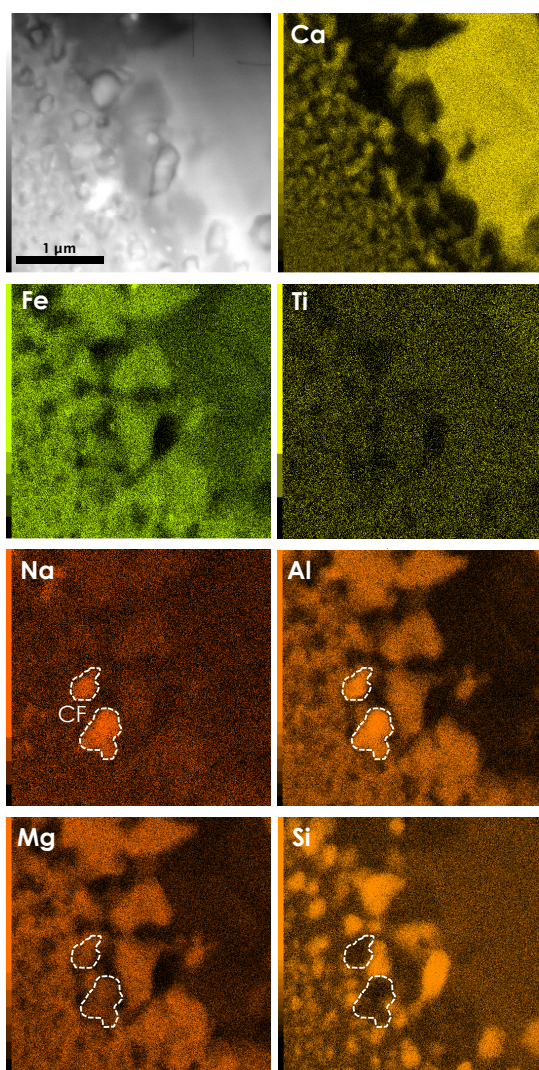


**Fig. S3.** TEM STEM elemental maps and electron images of the melting experiment of natural basalt (#2\_basalt at 64 GPa). The regions of interest show the interface between Ca-pv liquidus phase and the subsolidus assembly on the cold edges of the sample with mainly bridgmanite and stishovite matrix. The two highlighted crystals represent the hexagonal new Al-rich phase (NAL) which at the conditions of this experiment corresponds to the high-pressure polymorph orthorhombic Ca-ferrite-type phase (CF) (e.g. Dai et al 2013). The Na- and Al-enrichment is clearly visible on the chemical map. The CF-structure has also been captured by the *in situ* diffraction patterns in Fig. 2

666 **Appendix D.**

Chemical compositions of the resulting melt and coexisting phases presented in the literature

Run	Pradhan et al 2015				Tateno et al 2018									
	58		101		CP01		CP02		CP03		#75		#71	
P (GPa)	58		101		32		52		69		72		135	
T (K)	2570		2940		2570		2940		3280		3700		4300	
Phase	melt	MgPv	melt	MgPv	melt	CaPv	melt	CaPv	melt	CaPv	melt	CaPv	melt	CaPv
SEM/EPMA/TEM-EDS (wt%)														
SiO <sub>2</sub>	47.47	49.82	41.79	39.44	45.16	45.26	44.84	48.77	46.78	49.49	44.26	50.95	42.6	51.86
TiO <sub>2</sub>	2.53	0.84	4.88	1.46	1.92	0.77	1.78	0.84	1.68	0.65	2.14	0.7	2.45	0.66
Al <sub>2</sub> O <sub>3</sub>	18.62	15.6	20.01	17.09	15.12	4.22	20.48	2.11	21.98	1.7	18.29	2.65	17.95	1.73
FeO	13.2	10.57	17.79	16.46	15.09	1.71	13.79	1.95	13.69	1.94	14.58	2.42	16.7	2.58
MnO											0.21	0.09	0.24	0.05
MgO	6.64	20.58	3.56	23.57	10.55	2.34	9.2	2.52	8.12	2.3	9.03	3.26	7.05	2.9
CaO	9.04	0.91	8.5	0.4	6.03	38.08	5.53	35.96	5.22	36.06	4.53	35.63	3.84	38.27
Na <sub>2</sub> O	2.35	0.8	1.23	0.34	3.17	0.41	2.79	0.46	2.49	0.47	2.35	1.22	1.43	1.37
K <sub>2</sub> O	0.262				1.18	0.28	1.18	0.68	1.06	0.86	0.16	0.22	0.1	0.59
Cr <sub>2</sub> O <sub>3</sub>											0.12	0.02	0.15	0
Total	100.112	99.12	97.76	98.76	98.22	93.07	99.59	93.29	101.02	93.47	95.55	97.16	92.51	100.01

667

668 **Table S1.** Chemical analyses of the melts and coexisting phases presented in the literature.

669

670

671 **Appendix E.**

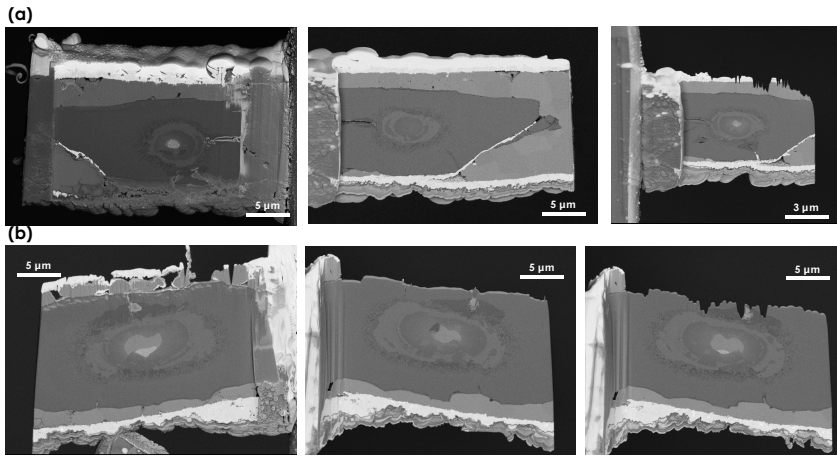


**Fig. S4.** Backscattered electron (BSE) images of two sides of the lamellas extracted from the quenched LH-DAC experimental samples recovered from high pressure and high temperature at different stages of milling. Panel **(a)**: #8\_M3\_1 65.5 GPa; **(b)**: #2\_basalt at 64 GPa. Both experiments were performed in KCl pressure medium. In the left side we show one side of the extracted lamellas with all the main phases described in the manuscript, in the central pictures the second side is shown before thinning down and indeed some of the observed features are missing and only after thinning further (pictures in the right side), we clearly see the same features as on the first side (pictures on the left) We show both sides of the extracted lamellas to emphasise firstly the fact that our experiments were fully encapsulated by the unreacted basaltic glasses (starting material) and to express the importance of finding the centre of the hotspot for reliable chemical analysis. The scale bar in (a) applies to all four images